PARAMETRIC DESIGN AND OPTIMIZATION OF A PIVOTING S-TYPE RUDDER FOR CONTAINERSHIPS

Chen-Wei Chen
Ocean College, Zhejiang University, Zhoushan, China.

Tsung-Yueh Lin
CR Classification Society, Taipei City, Taiwan, R.O.C, tylin@crclass.org

Bo-Yen Chen
Department of Engineering Science and Ocean Engineering, National Taiwan University, Taiwan, R.O.C.

Jen-Shiang Kouh
Ocean College, Zhejiang University, Zhoushan, China

PARAMETRIC DESIGN AND OPTIMIZATION OF A PIVOTING S-TYPE RUDDER FOR CONTAINERSHIPS

Chen-Wei Chen[1], Tsung-Yueh Lin[2], Bo-Yen Chen[3], and Jen-Shiang Kouh[1]

ABSTRACT

This study proposes an energy-saving S-type rudder design to deal with the inhomogeneous inflow from a rotating propeller behind a containership. The S-type rudder was modelled parametrically using four-digit NACA foils as section profiles together with Non-uniform rational B-splines (NURBS) surface formulations. A three-stage optimization process is proposed to reduce the number of design iterations necessary to achieve an optimal design. The propulsion simulations were done via CFD software, which solves the hydrodynamics of viscous flow, as governed by the Reynold-averaged Navier-Stokes (RANS) equations. Validations were performed with experimental model tests, including hull resistance, propeller open-water performance, and propulsion in calm water. Finally, energy recovery for different operational conditions is controlled by an innovative pivoting mechanism. The results show that the optimized S-type rudder can reduce delivered horsepower by 1% to 3%.

I. LITERATURE REVIEW

Wake-adapted rudders usually encounter several design issues, including high-dimensional design space, surface smoothness, complexity of wake field regarding hull and propeller effects, and long evaluation times. These drawbacks limit design explorations for an optimal shape. This study derives a high-order parametric rudder surface model and provides an optimization strategy to mitigate the time-consuming design process.

Energy-saving devices (ESDs) design has mostly been focused towards optimized hydrodynamic interaction between hull form, propeller and rudder to reduce operational cost. Various types of ESDs are being developed to enhance ship hydrodynamic performance from several standpoints, including improving resistance Park et al. (2015), improving propulsion by Kim et al. (2015), Friedrich and Uwe (2006) and Tahara et al. (2006), preventing cavitation on propeller blades and rudder surfaces by Thomas and Heinrich (2009), enhancing manoeuvring ability in deep and shallow water by Carrica, Castro and Stern (2010), etc.

Ship powering energy efficiency analysis and design often require self-propulsion experiments performed in a towing tank and/or by a free-running model for prediction of velocity-dependent effective wake, thrust deduction, relative rotative efficiency and hull efficiency Carlton (1994). Carrica et al. (2010) and Castro et al. (2011), adopted computational fluid dynamics (CFD) with innovative success to predict the self-propulsion and powering characteristics of a Korean container ship (KCS). Carrica et al. (2010) employed a six degrees of freedom motion model in the ship-fixed frame, with computations performed by the CFDShip-Iowa v4 code, employing a single-phase level set approach to solve the viscous flow with the free surface in the inertial frame, using either RANS or detached-eddy simulation (DES) models for turbulence, with the two-parameter blended k-ε/k-ω SST model. The computations of Castro et al. (2011) were performed with the wall function, using a blended k-ω/k-ε based DES turbulence model for their KCS self-propulsion simulations. Gaggero et al. (2017) presented a coupled BEM-RANS approach for KCS self-propulsion simulation with inviscid propeller body forces. On the other hand, Park et al. (2015) proposed several ESDs to improve the propulsion performance of the KVLCC2 container ship to satisfy the requirements of the energy efficiency design index (EEDI), as formulated by the International maritime Organization (IMO). Kim et al. (2015) proposed, using CFD verified with model tests, two ESDs, namely WAFon and WAFon-D, mounted in the pre-propeller plane to enhance the propeller inflow and reduce the loss of swirl energy in the slipstream.

Energy saving is crucial for large ships. One way to reduce energy is with proper streamlining of the hull form to reduce the resistance, Grigoropoulos and Chalkias (2010), Kim et al. (2016), and another way is to improve the propulsive efficiency Kim et al. (2015). Carlton (2012) showed that zones for ESD implementations can be classified as pre- Chang et al. (2018), in- Chen et al. (2014), Çelik and Güner (2007), and post-propeller

Fig. 1. Inflow velocity and force diagram for rudder.

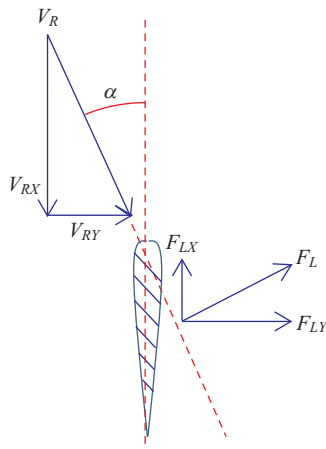**Fig. 2. Classification of the total wake velocity at any point in propeller plane.**

Fig. 3. Particulars of rudder.

plane, such as in this study, and the goal is to recover the energy losses from the propeller. HSVA Friedrich (2006) categorized these losses into frictional losses, rotational losses, axial jet losses, and hub vortex losses. The rotational losses can be measured behind the rotating propeller. A rudder, as an essential manoeuvring device, can also aid in energy recovery by generating a forward thrust component that is not parallel to the x-axis inflow, as shown in Fig. 1.

However, the reality is far from simple. The complex and inhomogeneous flow field after the hull and propeller typically causes challenges for the rudder to adapt to the wake. Thus, a design objective for S-type rudders in the spanwise direction is to enhance the propeller efficiency without, in the process, sacrificing the manoeuvrability. Some research neglects the presence of the hull and takes the average circulation distribution over the radius for design criteria. Other research employs the lifting line theory to design the rudder's spanwise profile resulting in jagged surfaces.

The wake is a key issue for rudder design as it is the outcome of interactions of hull, propeller and rudder. For a bare hull towed in calm water, the nominal wake can be measured in the propeller plane, and due to the symmetry of the hull, it is also symmetric about the centreline. When a propeller rotates behind the hull, the nominal wake is converted into effective wake, which is no longer symmetric because of rotation, and the propeller induces axial and tangential velocities in its own plane. Theoretically total wake velocity in the propeller plane behind a ship in calm water is the sum of effective velocity and propeller-induced velocity, as shown in Fig. 2, where the wave-induced velocity is neglected in the present study. So far those velocity items are axially or longitudinally dominated, which provide fast inflowing kinematic energy to the rudder. However the slip stream behind the propeller contains a rotational component, which may also be described as lateral components in the 12 and 6 o'clock positions. Furthermore a rudder as a lifting body, like a propeller, also induces velocity in its plane, and considerably affects the performance of the propeller. Indeed it is crucial that the rudder sections be designed to adapt to the inhomoge-
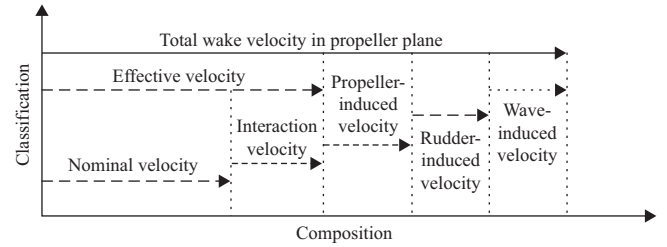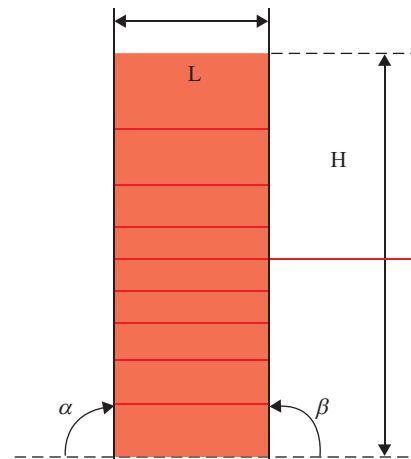
neous and deflected inflow.

This study initially used parametric geometry design for streamlining and smoothness, using the non-uniform rational B-splines (NURBS) technique. The geometric parameters were calibrated to adapt to the wake field based on the self-propulsion simulation of a containership and a five-bladed fixed-pitch propeller. Energy recovery for different operational conditions is controlled by an innovative pivoting mechanism. Based on computational fluid dynamics (CFD) simulations, optimization was performed to determine the best rudder geometry for improving the propulsive efficiency.

II. GEOMETRY MODELLING AND OPTIMIZATION STRATEGY

1. Parametric Twisted Rudder

To design a rudder, we firstly consider its principal dimensions: rudder depth H, chord length L, rake angles α and β, and foil sections, as illustrated in Fig. 3. A simplified model was selected using constant chord length L without rake (α and β are right angles), i.e., from the side view it is a rectangular projection. The depth H was set as the diameter of the propeller. The section profile was defined by the NACA 4-digit equations, Abbott and Doenhoff AEv (1960). The first digit is the camber ratio m, the second is the maximum camber position p, and the third and fourth represent the thickness ratio T. The foil is con-
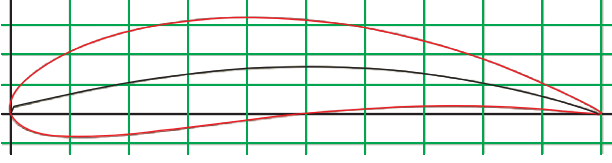
Fig. 4. NACA 8518 airfoil profile.

structed by the camber and thickness functions, as defined by Eqs. (1)-(3). For simplification, the mean line was set symmetric ($p = 0.5$) and the thickness ratio T was 18%; in other words each section was NACA x518, where camber ratio m varies with depth, as shown in Fig. 4 for $m = 8$.

$$y_c = 4m(x - x^2), \ 0 \le x \le 1 \text{ when } p = 0.5 \qquad (1)$$

$$yt = \frac{T}{0.2}(c_1 x^{0.5} + c_2 x + c_3 x^2 + c_4 x^3 + c_5 x^4),$$

where

$$c_1 = 0.2969, \ c_2 = -0.1260, \ c_3 = -0.3516, \qquad (2)$$
$$c_4 = 0.2843, \ c_5 = 0.1036$$

$$\begin{cases} \text{Upper}: x_u = c_x - y_t \sin\varphi \quad \text{and} \quad y_u = y_c + y_t \cos\varphi \\ \text{Lower}: x_l = x_c + y_t \sin\varphi \quad \text{and} \quad y_l = y_c + y_t \cos\varphi \end{cases},$$

where

$$\varphi = \tan^{-1}\left(\frac{dy_c}{dx}\right) \qquad (3)$$

The lift coefficient at each foil section is determined by the angle of attack and camber ratio. Since the wake flow after the propeller is irregular, the design of a wake-adapted rudder should consider various inflow conditions. The camber ratio m along the depth direction can be modeled by a cubic B-spline curve, i.e., a fourth-order curve, with 7 control points (CP) labeled P_0 to P_6. The B-spline curve $P(t)$ is defined by Eqs. (4) and (5) recursively for $k = 0, 1, \ldots, 6$, and the degree of the basis function is three; in the other words the order of spline $n = 4$. Fig. 5 shows the B-spline curve and the control points. The Z-axis is the depth direction, and the Y-axis represents the direction of camber. The middle CP P_3 (d_y, d_z) is located at the inflection point of the S curve, so that $d_y = 0$. The two CPs above the center CP and the two below the center CP control the magnitude and concentration of the S shape. To maintain the vertical tangential direction of the curve at the end points, a_y, b_y, f_y, and g_y are zero. The two end points were fixed at one radius from the propeller axis. Normalizing the above parameters, three
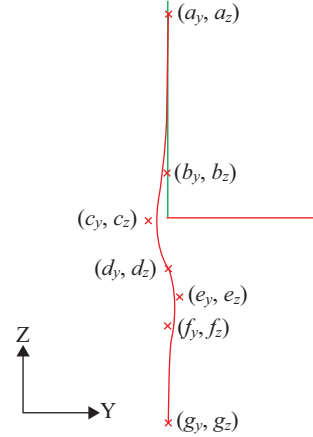

Fig. 5. Cubic B-spline curve with 7 control points.

design variables were identified to model the camber ratio distribution curve: the ratio of the z-coordinate of the center CP to the rudder depth M, the concentration S, and the magnitude Y, which are defined by Eq. (6). If $Y = 0$ the rudder is reduced to the original shape.

$$P(t) = \sum_{k=0}^{6} P_k N_{k,n}(t) \qquad (4)$$

$$N_{k,n}(t) = \left(\frac{t - t_k}{t_{k+n-1} - t_k}\right) N_{k,n-1}(t) + \left(\frac{t_{k+n} - t}{t_{k+n} - t_{k+1}}\right) N_{k+1,n-1}(t) \qquad (5)$$

$$M = \frac{d_z}{H}, \ S = \frac{c_z - e_z}{c_y - e_y}, \ Y = \frac{c_y}{H} - \frac{e_y}{H} \qquad (6)$$

The pivoting mechanism controls the twist angles of each section about the trailing edge, thereby creating an S-shaped leading edge. This includes one fixed axle attached to the trailing edge and one sliding axle along the chord-wise axis. The sliding axle passes through the camber lines of every section, as per Fig. 6. For the given camber lines and the pivot position C, the twist angles of each section are determined. As C increases, the sliding axle is closer to the fixed axle, and the overall twist angles become larger, which better suits the condition of increased rotational flow. This mechanism provides a single parameter to control the twist angles. Full mathematical formulation of the rudder surface is included in the appendix. Table 1 lists the geometric parameters for an S-type rudder and the four design variables M, S, Y and C that are going to be optimized and described in the next section. The wetted surface area of the rudder takes about 1% of the ship hull at the design draft.

2. Optimization Algorithm

To investigate the performance of a rudder in propulsion scenarios we have to consider the following aspects: ship resistance and wake, propeller effects, and the rudder hydrodynamics itself,

Table 1. Geometric parameters for an S-type rudder.

Type of variable	Symbol	Value
Principal dimension Model scale ($\lambda = 31.6$)	H	0.25 m
	L	0.158 m
	α	90°
	β	90°
	Wetted surface area	0.0883 m^2
Foil section NACA 4-digit Series	p	0.5
	T	0.18
Design variable	M	To be optimized
	S	To be optimized
	Y	To be optimized
	C	To be optimized
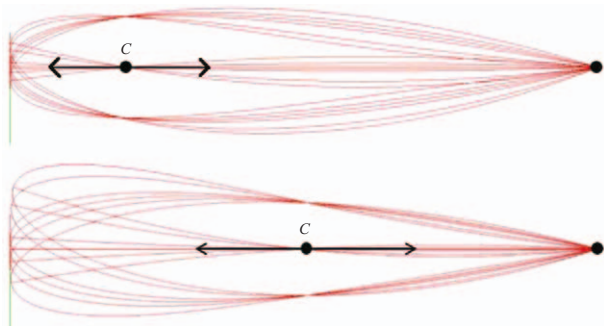
Fig. 6. Pivot axle passing through the camber curves for each section.

i.e., the hull-propeller-rudder interaction. Changing the shape of the rudder will alter the overall resistance and hence introduce a change of propeller rotation speed to the adopted self-propulsion condition. The modification of the rudder causes complex and comprehensive changes in all aspects of the propulsion, which requires redoing simulations for each design. This analysis takes too much effort and time to conduct a global optimization, even for this 4-variable optimization problem, since it involves grid regeneration and CFD simulation. So the optimization in the present study is intended to be a local optimal solution, and since there is no gradient information provided by the objective function, a non-gradient searching algorithm was used.

The objective function is to minimize the delivered horse power, *DHP*, at self-propulsion condition, which is defined by Eq. (7), where n_{sp} is the rotation speed of the propeller at self-propulsion condition and Q is the torque of the propeller. The self-propulsion condition is defined as the balance of forces of total resistance and thrust, as per Eq. (8), where R_{hull} and R_{rudder} are the resistances of the hull and rudder and also in terms of propeller rotation speed. R_W and *SFC* are constants for wave-making resistance and skin friction correction. Here it should be emphasized that R_{hull} is the hull resistance without wave-making effect but with propeller-induced suction pressure. T is the thrust force generated by the propeller at n_{sp}. For each rudder

design, n_{sp} is calculated to satisfy Eq. (8) and then *DHP* is obtained. We will elaborate the decomposition of resistance and propulsion simulation in the later section describing the CFD configurations.

$$DHP = 2\pi n_{SP}Q(n_{sp}) \tag{7}$$

$$R_{hull}(n_{sp}) + R_w + R_{rudder}(n_{sp}) - SFC = T(n_{sp}) \tag{8}$$

The four design variables, *M, S, Y* and *C* are classified into two categories: parameters for camber distribution *M, S*, and *Y*; and the parameter *C* affecting the overall twist angle. The constraints for *M*, the location of the twist inflection point, were -0.16 and -0.10, according to the wake survey of this ship that the center is below the propeller axis. The concentration factor *S* was set between -3.5 and -1.0 to cover the twist range from the twist center to half depth. The camber magnitude *Y* was set between 0.01 and 0.07, which are common camber ratios for foil designs. The pivot position *C* was between 0.3 and 0.7 times the chord. The starting parameter set $\{M, S, Y, C\}^0$ was {-0.10, -1.0, 0.04, 0.5}, where the superscript denotes the number of design iterations.

The optimization was divided into three sequenced stages due to the high costs of every evaluation. The first stage was for *M*, the second for *S* and *Y* simultaneously, and the third for *C*. Within each stage, variables outside the considered stage were kept constant, so that the degree of design space could be reduced to one dimension for the first and third stages, and two dimensions for the second stage, as per Fig. 7. The searching method was uniform grid for each given constraint. The step sizes for *M, S, Y*, and *C* were 0.01, 0.5, 0.01, and 0.1 respectively. The concept for this arrangement is to solve for the most independent variable first. An adopted rudder design is based on the inflow condition, of which the flow directions hardly change, while the distribution of velocity magnitude varies with ship and propeller speeds. After those distributional parameters are resolved, the most effective parameter *C* is then optimized. This algorithm identifies the key geometrical parameters that have di-

Table 2. Principal dimensions of target ship.

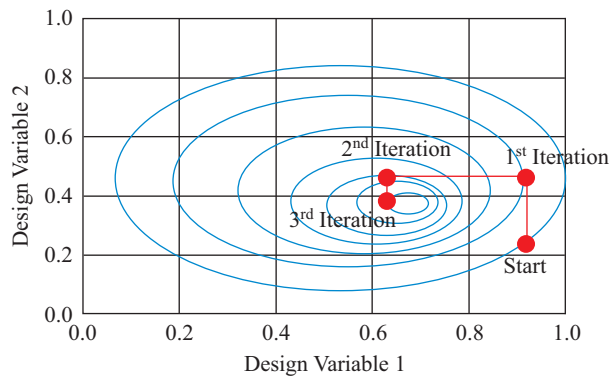| Item	Particulars	Ship scale	Model ($\lambda = 31.6$)
KCS Containership	Design speed	24 knots	2.196 m/s
	Length overall L_{OA}	230 m	7.28 m
	Breadth	32.25 m	1.02 m
	Depth	19.0 m	0.601 m
	Design draft	10.8 m	0.342 m
	Displacement	52030 m^3	1.649 m^3
	Wetted surface area	9424 m^2	9.438 m^2
KP505 Propeller	Propeller diameter	7.9 m	0.25 m
	Hub diameter	1.422 m	0.045 m
	Expanded area ratio	0.8	0.8
	P/D at 0.7 radius	0.95	0.95

Fig. 7. Two-variable gradient search algorithm.
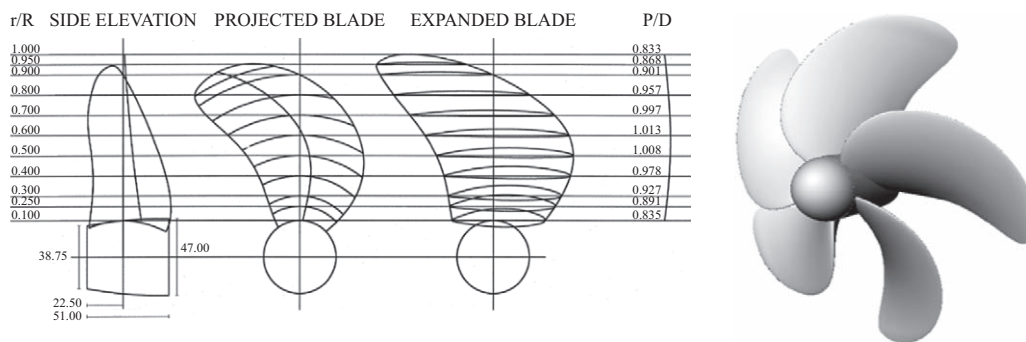

Fig. 8. KCS hull form.

Fig. 9. KP505 propeller layout and geometry.

rect effects on the propelling power. The benefit of the proposed pivot design concept is in identifying the most influential single variable for optimization purposes, not only for the design speed, but also applicable to various ship speeds.

III. COMPUTATIONAL MODEL

1. Containership Model

A 230 m containership (KCS) and its screw propeller (KP505) designed by KRISO Corp. in Korea were adopted for this research, as shown in Figs. 8 and 9. Since the finite volume method (FVM) was selected as the numerical solver, a finite computation domain was determined. For the external flow, the domain boundaries were chosen according to the object geometries, including the hull form, propeller, rudder, and undisturbed far field. The principal dimensions of the hull form and the propeller are

included in Table 2. The simulation scale was selected based on the model scale tested in a basin to validate the results.

2. Numerical Method for Propulsion

The characteristics of the hydrodynamic loads induced by the ship propulsion system were studied by numerical simulations. For Newtonian fluids, the flow field must satisfy the conservation of mass, momentum, and energy. Because of the low Mach number, i.e., lower than 0.3, and near constant temperature of the surroundings for marine environments, it is appropriate to assume that the fluid is incompressible, viscous, and isothermal. This simplification leads to the Navier-Stokes equations, Launder and Spalding (1974). Reynolds' number for ships is usually above 5.0×10^6, so the flow field is considered to be fully turbulent. By decomposing the velocity and pressure terms into mean and fluctuating parts, which was first derived by Reynolds (1895), the continuity and momentum equations yields the Reynolds-averaged Navier-Stokes (RANS) equations as shown in Eqs. (9) and (10). In these equations, u_i is the velocity vector, p is the pressure, g_i is the gravity, and v is the dynamic viscosity. The commercial CFD package CD-Adapco Star-CCM+, a general purpose RANS solver, was applied to simulate the flow field around the target ship. The two partial differential equations are solved by the FVM. To solve coupled variables, the numerical scheme utilizes a segregated method, called SIMPLE, to decouple the pressure and velocity terms. For the free surface, it is necessary to simulate two types of fluids with no chemical reaction and no phase change between them, Dawson (1977) and Robert et al. (2003). For such conditions, CFD utilizes the VoF method, which mixes the two fluids by a volume fraction. The properties of the mixture are interpolations of the densities and viscosities of the two fluids, which is subsequently substituted into the Reynolds transport equation to solve for the material convection. The interface is defined on the iso-surface for volume fraction equal to 0.5, representing half water and half air.

$$\frac{\partial \overline{u}_i}{\partial x_i} = 0 \tag{9}$$

$$\frac{\partial \overline{u}_i}{\partial t} + u_j \frac{\partial \overline{u}_i}{\partial x_j} = -\frac{1}{\rho}\frac{\partial \overline{p}}{\partial x_i} + \frac{1}{\rho}\frac{\partial}{\partial x_j}\left[\mu\left(\frac{\partial \overline{u}_i}{\partial x_j} + \frac{\partial \overline{u}_j}{\partial x_u}\right)\right]$$
$$-\frac{\partial\left(\overline{u_i' u_j'}\right)}{\partial x_j} + g_i \tag{10}$$

The computational domain of the numerical model is shown in Fig. 10. The computational domain was set by boundary conditions. The characteristic lengths of the ship determined the size of far field domains. Four times L_{OA} to avoid wave reflection for side walls, one time and two times L_{OA} in the forward and backward directions respectively, and one time L_{OA} in the depth di-
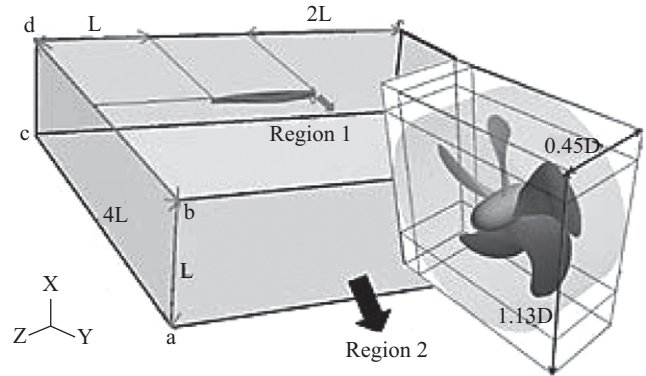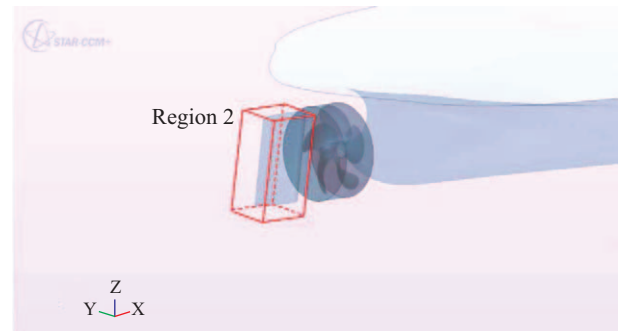

**Fig. 10. Computational domain of propulsion test.**

Fig. 11. Computational domain of propulsion with rudder appendage.

rection. The velocity inlet specifies the velocity vector on the front and bottom boundaries. The pressure outlet specifies the hydrostatic pressure with backflow correction on the back plane. The no-slip walls specify zero velocity on the hull surfaces. The slip wall specifies non-permeable conditions on the side far fields and top plane. The grids representing the propeller and the interface wrapped around the propeller utilized the moving reference frame (MRF) technique, which involves rigid body motions between the hull, rudder and propeller, as shown in Fig. 11. The boundary conditions for the different simulations are listed in Table 3.

The traditional approach, using the Froude method, extrapolates the hull resistance from the model to the full-scale ship. This is not physically correct because the viscous pressure drag is dependent on Reynolds' law. In the numerical simulation, the double body-model assumes that, for a floating body, the immersed part has a mirrored image (or doubled) with respect to the undisturbed flat free surface, so that the flow field is symmetrical. The configuration guarantees that streamlines lie on the symmetry plane, i.e., that there is no wave formation and no wave-making resistance. When the double-body model is selected, the resistance represents the viscous resistance R_v. Comparing R_v to the flat-plate resistance R_{FP} defined by ITTC-57, the additional viscous pressure drag is regarded as the form factor K. Subtracting R_v from the total resistance R_T, we obtain the wave-making resistance R_w, which is considered with little scale

Table 3. Boundary conditions.

Boundary condition type	Applied boundary		
	Resistance	Open-water	Propulsion
Velocity inlet	Front, Top, Bottom	Front	Front
Pressure outlet	Back	Back	Back
No-slip wall	Hull	Propeller, Hub	Hull, Propeller, Hub
Slip wall	Far side	-	Far sides, Top, Bottom
Symmetry	Centreline plane	Far sides	-
Interface	-	Cylinder (MRF)	Cylinder (MRF)
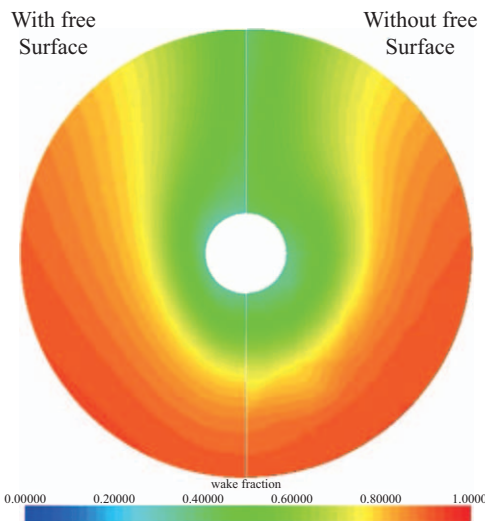
Fig. 12. Nominal wake distributions at propeller plane.
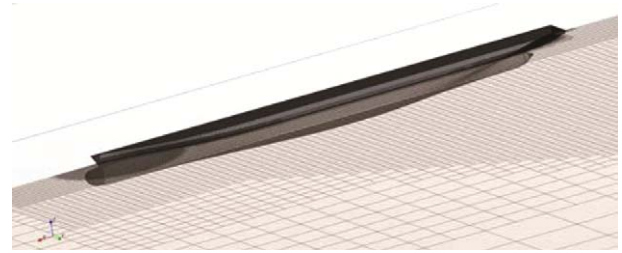
Fig. 13. Grid around hull and free surface.
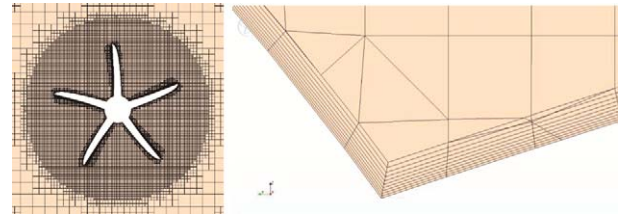
Fig. 14. Propeller grid and prism layer.

effect. So the total resistance can be decomposed into two terms and non-dimensionalized as Eq. (11). R_w and K are used at propulsion simulations.

$$R_T = R_w + R_v = \frac{1}{2}\rho V^2 S_0 \left[C_w + (1+K)C_{FP} \right] \qquad (11)$$

This property is beneficial to the simulations without using the VoF method at the same Froude number as the dense grid near the free surface can be removed and the computational time thereby reduced. Fig. 12 compares the nominal wake distributions from the bare hull resistance simulations with and without free surface. It is shown that they produce very similar inflow conditions for the propeller. In a propulsion test, if the influence of the free surface on the propeller operation is neglected, the same technique applies without the concerns of altering the wakes.

3. Verification and Validation

The unstructured grid strategy includes two algorithms: prism layer and Cartesian grid. The prism layer grid is controlled by y^+ spacing, which matches the wall function to resolve the shear stress. The Cartesian grid is controlled by X, Y, and Z direction spacing, independently. Grid generation was completed according to the following rules and shown as Figs. 13 and 14:

(i) Refined grids around the bow and stern regions.
(ii) Fine grid near the disturbed free surface to resolve the wave pattern.
(iii) Prismatic layers generated on the no-slip walls.
(iv) Refined grid in the axial direction in the wake region.

Grid independency tests were conducted by adjusting relative grid sizes and the number of prism layers until the pressure and shear resistance approached the desired value. Tables 4 and 5 show the variations with grid number (*GN*), and the medium grid with 10 prism layers was selected with less than 1.0% resistance variation. The open water simulation was performed in the same manner, so that K_T and K_Q variations were less than 1.0%. The grid arrangement for the propulsion simulation combined the previous two, but without the very fine free surface grid.

The experimental results of the resistance test are available at its corresponding design speed $V_s = 24$ knots. It was conducted in captive mode, which fixed the hull at the design draft. Table 6 shows the CFD results compared with the experimental results.

Table 4. Grid independency test-base size.

Base size	GN (millions)	R_{vp} (N)	Difference
Coarse	3.58	9.22	-
Medium	4.08	9.20	0.22%
Dense	6.85	9.19	0.11%

Table 5. Grid independency test-prism layer.

Layers	GN (millions)	R_f (N)	Difference
4	0.91	32.12	-
7	0.95	31.43	2.71%
10	1.23	30.82	0.72%

Table 6. Resistance and propulsive coefficients.

	EXP	CFD	Error
C_T ($\times 10^{-3}$)	3.55	3.506	-1.24%
$1-w_n$	0.686	0.729	6.27%
C_W ($\times 10^{-3}$)	0.561	0.534	-4.81%
$1 + K$	1.1	1.092	-0.73%
n (rps)	9.5	9.522	0.23%
K_T	0.172	0.173	0.58%
K_{Qb}	0.0288	0.0297	3.13%
$1-t$	0.853	0.815	-4.45%
J	0.728	0.719	-1.24%
$1-w_e$	0.792	0.779	-1.64%
η_h	1.077	1.045	-2.97%
η_r	1.011	0.999	-1.19%
η_o	0.682	0.663	-2.79%
η_p	0.743	0.691	-7.00%
DHP (ps)	0.206	0.214	3.98%
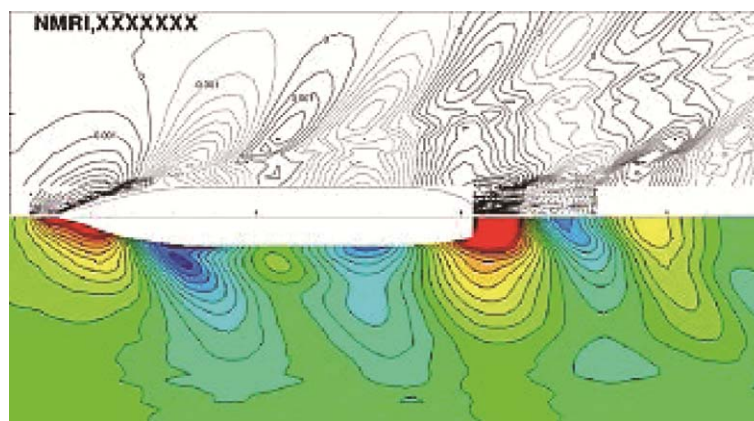
Fig. 15. Wave pattern at 24 knots.

The C_T value was 1.2% less than that from the experiment, while the nominal wake value was 6.27% larger due to over prediction at the inner radius by CFD. This may have been caused by the biased Reynolds' shear stress determined by the k-ε turbulence model. Figs. 15 and 16 show the wave pattern and the wake on the propeller plane at 24 knots. The divergent and transverse wave pattern systems were clear, and in comparison with the experimental results, both had similar forms. Subtracting R_v from R_T, the wave-making resistance R_w was 12.114 N, 4.8% less than the experiment. The form factor K was quite accurate, with less than 1% error.

The open-water test simulated the thrust and torque coeffi-

Table 7. Self-propulsion at 24 knots without and with rudder.

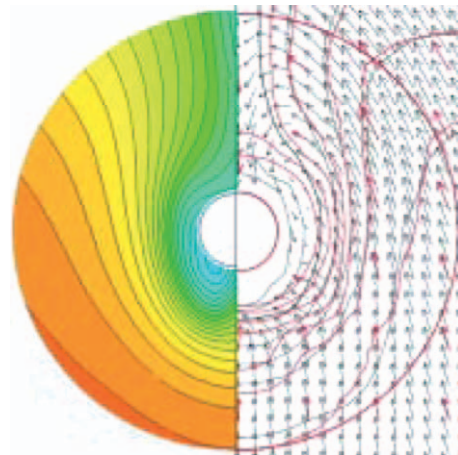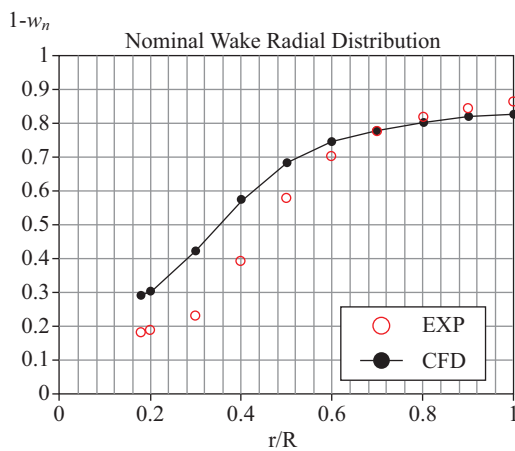|	w/o rudder	w/straight rudder
R_w (N)	12.114	12.114
SFC (N)	29.917	30.207
n (rps)	9.522	9.56
R_{hull} (N)	78.661	78.710
R_{rudder} (N)	-	1.231
T (N)	60.858	61.848
Q (Nm)	2.627	2.717
DHP (ps)	0.214	0.222

Fig. 16. Nominal wake field: CFD (left) and experiment (right).
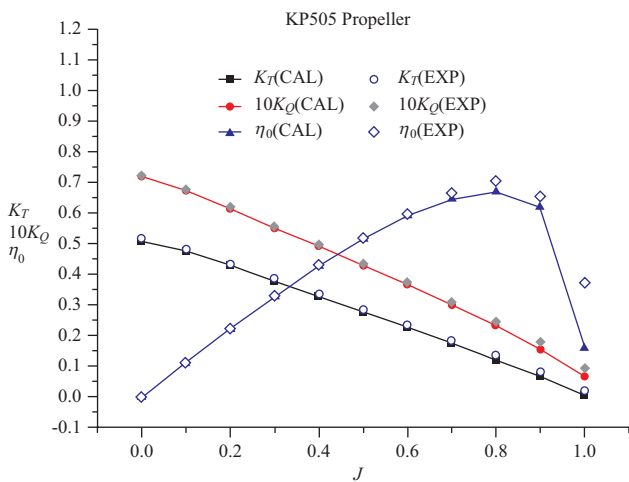

Fig. 17. KP505 open water performance.

cients, K_T and K_Q, and the efficiency η_o versus the advance coefficient, J, in uniform flow. J was increased in increments of 0.1 from 0.0 to 1.0. The K-J chart with the experimental results is shown in Fig. 17. K_T and K_Q from the CFD results agreed with the experimental results, and the efficiency η_o was precisely predicted except at high loading conditions.

The self-propulsion simulations were conducted without a rudder, as per the experiments. Table 6 lists the rotational speed n, K_T and K_Q at the self-propulsion condition, with the skin friction corrector SFC calculated by Eqs. (12) and (13). The model-ship correlation ΔC_F was taken the same as experiment, 0.27×10^{-3}. The algorithm for finding n_{sp} to achieve Eq. (8) was the Newton-Raphson method. The resultant n and K_T were found to be about 1% different from the experiment, while K_{Qb} and thrust deduction t suffered discrepancies from 3% to 5%, resulting in lower η_r and η_h respectively. On the other hand, the accuracy of the effective wake w_e was improved and the error was reduced to 1.6%. Despite the error of nominal wake possibly inducing uncertainties for the rudder analysis and optimization, this error was greatly reduced due to propeller effect. The propeller open water performance, i.e., the K-J chart was coincident with experiment, except that η_o was underestimated by 2.8%, and the overall propulsive efficiency η_p was 7% underrated. In terms of DHP, the error was reduced below 4%. In the propulsion simulations with rudder, the grid strategy, determination of self-propulsion condition, CFD configurations were kept strictly identical to avoid any additional errors to DHP, and its 4% error was considered as a systematic bias across all simulations. As the objective function only compares the relative minimum, the validated propulsion simulations were regarded to be sufficiently accurate for the use of optimization.
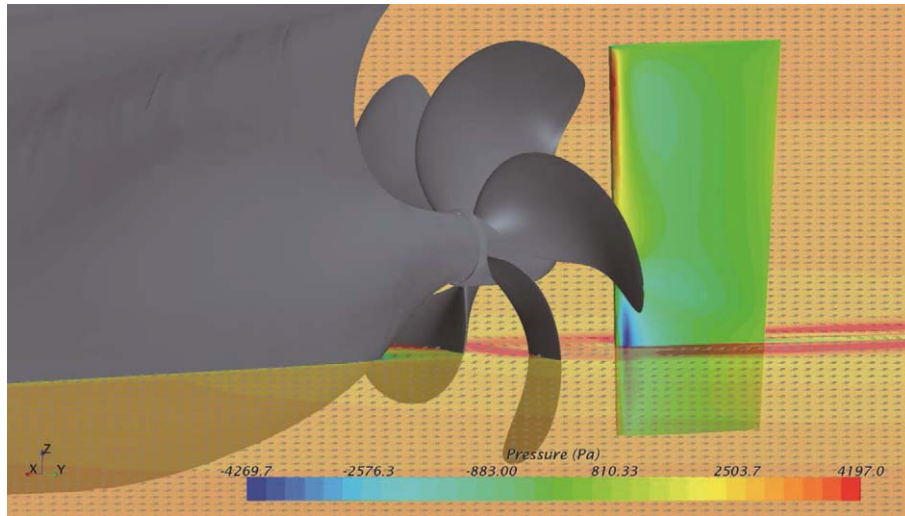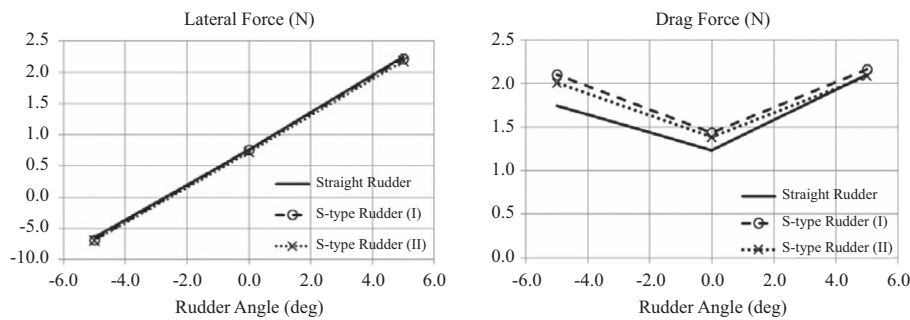
Fig. 18. Pressure on straight rudder at 24 knots.

Fig. 19. Rudder forces at different rudder angles.

$$SFC = \left\{ (1+K)(C_{FO_M} - C_{FO_S}) - \Delta C_F \right\} \times \frac{1}{2} \rho U^2 S_0 \quad (12)$$

$$C_{FO} = \frac{0.075}{(\log_{10} Re - 2)^2} \quad (13)$$

4. Rudder Placement in Propulsion

The addition of a rudder into the flow field causes changes from the beginning. First of all the overall wetted surface area increases and hence the resistance and *SFC* increase. Then the propeller rotates faster to provide additional thrust to overcome the drag of the rudder. The augmented resistance of the hull induced by the propeller suction then increases, and so on until the total resistance and thrust forces balance, reaching Eq. (8). What is not being affected is the wave-making resistance R_w, due to the rudder usually being placed with sufficient submergence so as to avoid free-surface effects. Table 7 shows the differences between those two conditions and Fig. 18 illustrates the velocity field and pressure contour around a straight rudder, placed at zero angle. One can easily see that the high pressure region above the propeller axis is on the port side, while below the axis it is on the starboard side. The propeller induces lateral inflow velocity components to the rudder unevenly. In terms of total forces on the rudder, Fig. 19 depicts the lateral and drag forces of three rudders, two of them arbitrarily chosen S-types, against different rudder angles from -5° to 5° under the same ship speed 24 knots and propeller speed 9.56 rps. This setup ensures identical inflow for various rudder designs so that the comparison can be on the same basis, but only the one with 0° achieved a self-propulsion condition. Here we should elaborate that the self-propulsion condition is not only in terms of longitudinal forces, but that the lateral force should also be zero when running straight. This requires the rudder angle being about -3°, and the change of drag further interrupts the original self-propulsion condition. So the simulation would take several times longer to achieve both criteria, and this would not be considered in the present study. On the contrary, Fig. 19 gives two good properties: the lateral force is hardly dependent on the rudder design, and the difference between drag forces for different rudders is almost invariant with rudder angle between 0° and -5°. These provide reasonable grounds to state that the optimal rudder will retain its minimization of drag among the design space if operating at -3° rudder angle. Therefore, the rudder placement in the optimization process was chosen as 0° and the achievement of self-propulsion condition followed Eq. (8).

Table 8. Self-propulsion without rudder at various speeds.

V_s (knots)	21	24	27
V_m (m/s)	1.9215	2.196	2.4705
R_T (N)	57.620	79.460	124.60
R_w (N)	5.092	12.114	40.940
SFC (N)	21.362	29.917	39.515
n (rps)	8.135	9.522	11.003
J	0.720	0.719	0.636
DHP (ps)	0.141	0.214	0.339
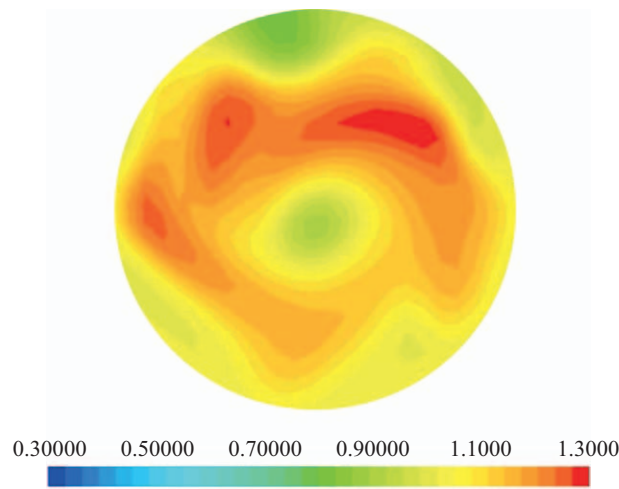
Fig. 20. Inflow velocity distribution in the rudder plane.
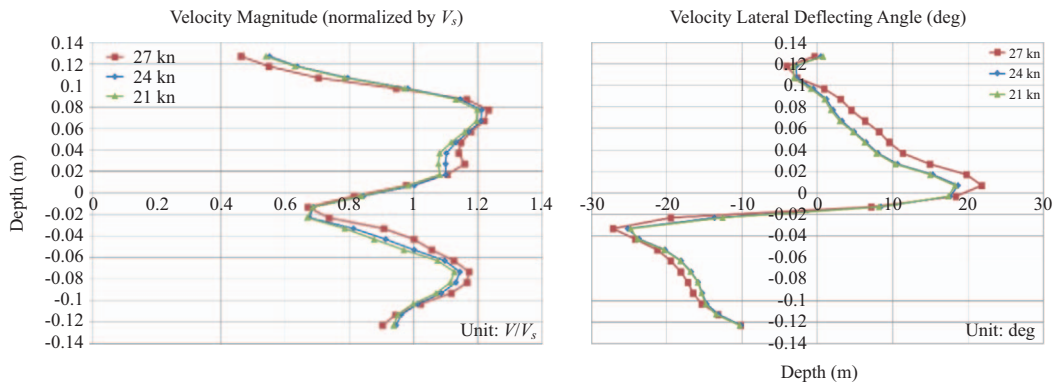
Fig. 21. Rudder inflow velocity along the depth at aft perpendicular.

IV. RESULTS AND DISCUSSION

1. Wake Field Analysis

To characterize the rudder inflow field and illustrate their similarities at different ship speeds, the propulsion simulations at V_s = 21, 24, and 27 knots without a rudder were conducted and each achieved the self-propulsion condition. Table 8 contains a resistance part and a propulsion part, providing the calculations of *SFC* and R_w. Fig. 20 shows the velocity magnitude behind the propeller on the rudder plane at 24 knots. The inhomogeneous distribution is the outcome of the hull, propeller, and their complex interactions. While the nominal wake is slower at the 12 o'clock position due to the boundary layer extended from the stern, the wake field running into the rudder is asymmetric in magnitude and direction. The inflow velocities along the aft perpendicular are shown in Figs. 21 and 22. From the results, the velocity is redirected by the propeller's rotation. The S-shape curve is present and the maximum magnitude of direction is above 25°. The twist region from positive to negative is concentrated near the propeller axis, and the center of twist is slightly below the propeller axis. The characteristics of this S-shaped curve correspond to the B-spline model of the camber ratio dis-
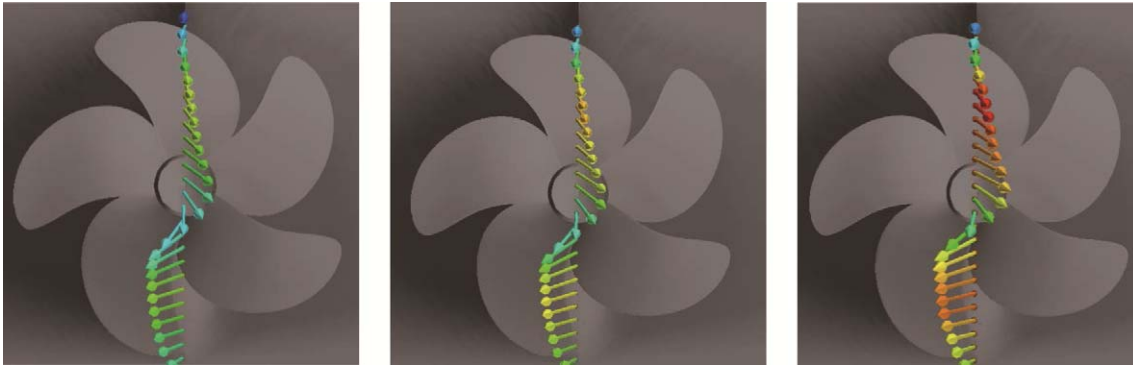
Fig. 22. Rudder inflow velocity direction along the depth at aft perpendicular.
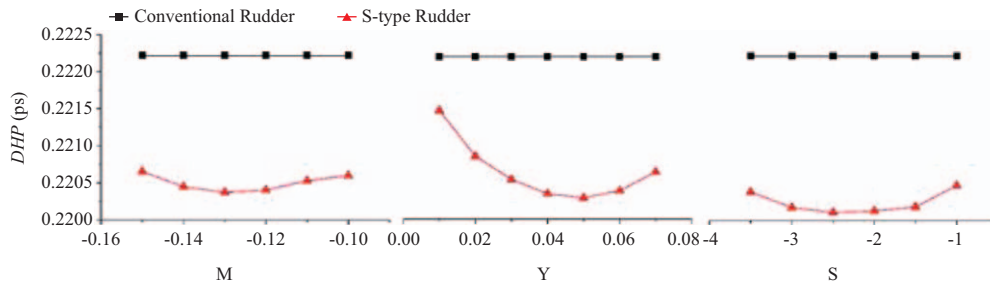

Fig. 23. Optimization of camber distribution: original and S-type (red).

tribution along the depth direction. On the other hand, there are similarities across various ship speeds. Fig. 21 plots the normalized magnitude of velocity and it is seen not to be relevant to the propeller loading, i.e., the advance coefficient J. However for higher speeds, a reduction in J introduced higher deflection angles to the rudder inflow. This would be the major function of the pivot position C adapting to inflow directions, while not affecting the other distributional parameters of camber.

2. Wake-adapted Camber Distribution

In this section the self-propulsion simulations were conducted with the conventional straight type and the twisted S-type rudder proposed in this study. The design speed V_s was 24 knots and was simulated with various rudders. For each combination self-propulsion condition was achieved. The local optimization process was divided into three stages: find the parameter M to locate the twist center, and then search for the optimal combination of concentration S and magnitude Y, and finally search for optimal pivot position C. The rotation speed n_{sp} was tuned to meet the self-propulsion condition, as per Eq. (8), of each design, and then DHP was obtained. The starting parameter set $\{M, S, Y, C\}^0$ was $\{-0.10, -1.0, 0.04, 0.5\}$. The first stage kept $\{M, S, Y, C\}^1 = \{M^1, -1.0, 0.04, 0.5\}$ and varied M^1 from -0.16 to -0.10. $M^1 = -0.13$ was found to minimize DHP to 0.2203 ps. The optimal twist center was located below the propeller axis, which complies with the flow analysis in Fig. 21. The second stage iterated S and Y, while keeping $\{M, S, Y, C\}^2 = \{-0.13, S^2, Y^2, 0.5\}$. This stage utilized a two-variable gradient search

algorithm that alternately fixed S and Y to determine the minimum until both variables are stable. S^2 was set as -1.0 with Y varied, for which Y^2 was found as 0.05. The third iteration began at $\{-0.13, S^3, 0.05, 0.5\}$, while keeping Y^3 constant. DHP was a minimum when S^3 was -2.5. Then the fourth iteration began at $\{-0.13, -2.5, Y^4, 0.5\}$, while keeping S^4 constant. The minimum of DHP occurred at $Y^4 = 0.05$, which returned to the second iteration as $Y^2 = Y^4$. It was regarded that the fourth iteration had converged for $\{M, S, Y, C\}^4$ at $\{-0.13, -2.5, 0.05, 0.5\}$, and the resulting DHP was 0.2201 ps. Compared to the non-twisted design, where DHP = 0.2222 ps, the optimized camber distribution can reduce DHP by 0.95%. Fig. 23 shows the local minimum of the optimization processes where the black line with square points represents the conventional rudder and the red line with triangular points represents the designed S-type rudder with significant variation of design parameters M, S, and Y against DHP.

3. Optimization for Various Speeds

The final stage was conducted at $V_s = 21$, 24, and 27 knots. From the previous wake analysis at various ship speeds, the normalized distribution of velocity magnitude hardly changed, and the distribution of the lateral deflection angle of inflow velocity followed the same curved shape, while slightly larger for higher speeds. This outcome gives reasonable grounds to maintain the optimized distributional parameters and vary the pivot position C to minimize DHP under various speeds. The determination of self-propulsion condition was the same as pre-
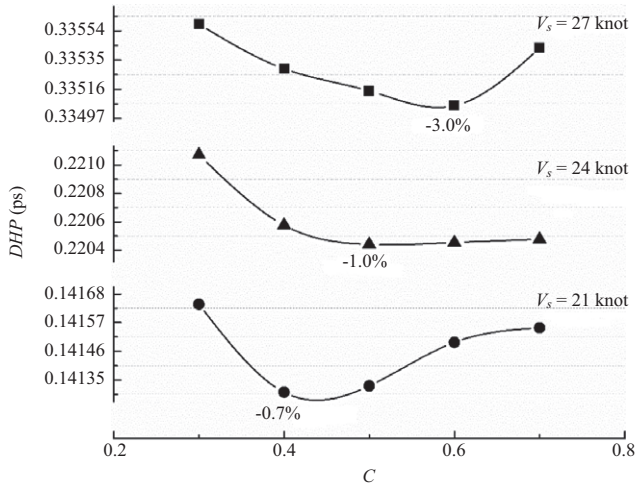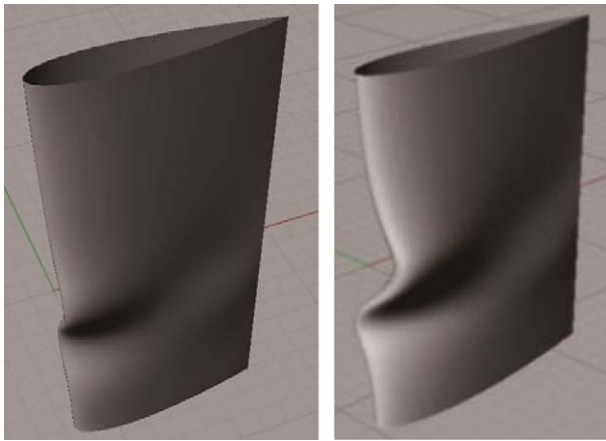
Fig. 24. Pivot location optimization for various speeds.

Fig. 25. Optimal S-type rudder for C = 0.42 (left) and 0.58 (right).

Fig. 26. Optimal S-type rudder for C = 0.58 and flow field.

viously stated. Fig. 24 shows the different optimal pivot positions and indicates the *DHP* reduction percentage compared to one with a conventional straight rudder. One can see the tendency that the optimal *C* increased, moving towards the trailing edge, for higher speeds, and so did the *DHP* reduction as well. The results showed that at 27 knots the optimal S-type rudder could recover up to 3% of *DHP*. The corresponding optimal rudder geometries for 21 and 27 knots, as *C* = 0.42 and 0.58, are shown in Fig. 25. The explanation of this geometrical tendency could be that when the propeller loading increases for higher speeds, it induces higher velocities in the lateral direction, which we can see from the wake analysis. Then adapting to the highly deflected flow field *C* should be increased to produce a more sharply twisted S-shape, which can be seen in Fig. 26. It is also due to the higher deflection of the inflow for the rudder, a well-pitched section could generate higher lift, and hence provide more thrust force in the longitudinal direction to mitigate the its own drag . So the power reduction can be raised for a higher speed if the pivot location is optimized for that speed.
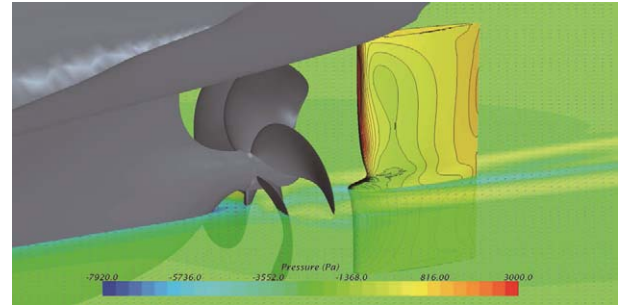
V. CONCLUSIONS

This study developed a parametric design model for S-type rudders. The design process not only guarantees surfaces that are smooth and streamlined, but also have sufficient freedom to adapt to complex wake fields. Four design variables were used in the optimization process, three of which control the camber distribution while the pivoting position controls the twist angle of each section. The objective function was evaluated using CFD software, which simulated the hull, propeller, and rudder interaction and found the required *DHP* under self-propulsion conditions. The optimization was performed in three stages to find the optimal rudder geometry to improve the efficiency. The pivot position was the only parameter to be tuned to optimise efficiency at various ship speeds. At design speed, 1% *DHP* can be recovered, while at 27 knots up to 3% *DHP* can be recovered. The calculation results and methodology in this study would be of great significance to large cargo ships with long straight-line voyages in terms of energy-saving design. In terms of lateral forces, the conventional and S-type rudders remained almost identical over a small range of rudder angles. In the future, hydrodynamic performance of large deflections of the S-type rudder should be estimated and integrated with manoeuvring testing studies.

APPENDIX

In the present study the S-type rudder is constructed section by section, which are predefined foil shapes. The parametric domain is $0 \le (s, t) \le 1$, where s is the chordwise direction and t is the depth direction, as shown in Fig. A-1. s and t begin at the trailing edge and upper most section respectively.

Definition of the camber and thickness lines of the NACA 4-digit series oriented in the X-Y coordinate system, where the
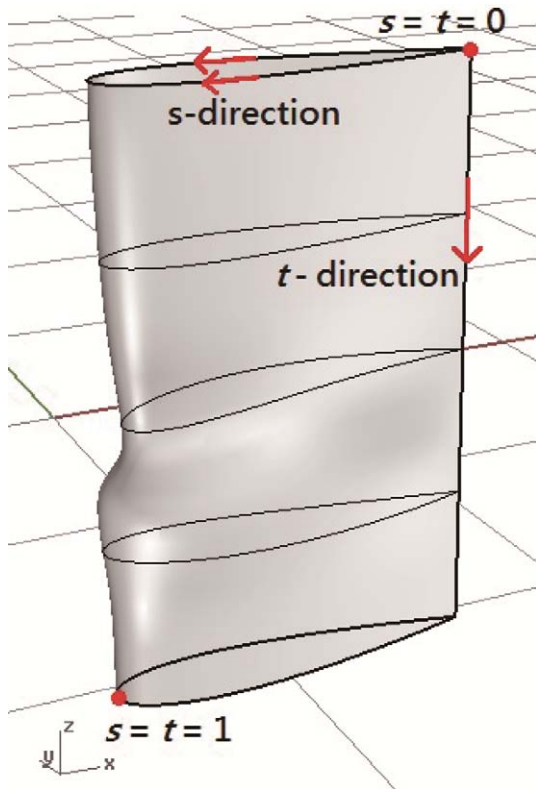
Fig. A-1. Pivot rotary of S-type rudder section foil in spanwise.

Fig. A-2. Definition of foil section and parameter.

about $x = 0.5$ and thus define a S-Y coordinate system, where $s = 1 - x$. This doesn't change θ. The point (x_p, y_p) is the intersection of the circle centered at $(1, 0)$ with radius C and the camber line:

$$\begin{cases} x^2 + y^2 = C^2 \\ y = 4m(x - x^2) \end{cases} \tag{A-5}$$

$$16m^2 x^4 - 32m^2 x^3 + (16m^2 + 1)x^2 - C^2 = 0 \tag{A-6}$$

The quartic equation can be solved analytically in the explicit form. Only one root x_p, which is real and between 0 and 1 is viable. When m is small compared to unity, the solution can be approximated by:

leading edge is located at the origin:

$$y_c(x) = 4C_{max}(x - x^2),\ 0 \le x \le 1 \tag{A-1}$$

$$(x_p, y_p) \sim [C, 4m(C - C^2)] \tag{A-7}$$

$$y_t(x) = \frac{T}{0.2}(0.2969x^{0.5} - 0.126x - 0.3516x^2 + 0.2843x^3 - 0.1036x^4) \tag{A-2}$$

And the twist angle θ is:

$$\begin{cases} \text{Upper}: x_u = x_c - y_t \sin\varphi \quad \text{and} \quad y_u = y_c + y_t \cos\varphi \\ \text{Lower}: x_l = x_c + y_t \sin\varphi \quad \text{and} \quad y_l = y_c + y_t \cos\varphi \end{cases}$$

$$\theta = \tan^{-1}\left(\frac{y_p}{x_p}\right) \sim \tan^{-1} 4m(1 - C) \tag{A-8}$$

where

The transformed upper and lower section points are scaled up to the chord length L:

$$\varphi(x) = \tan^{-1}\left(\frac{dy_c}{dx}\right) \tag{A-3}$$

$$(x'_u, y'_u) = L \begin{bmatrix} \cos\theta & -\sin\theta \\ \sin\theta & \cos\theta \end{bmatrix} \begin{bmatrix} x_u \\ y_u \end{bmatrix} \tag{A-9}$$

The section rotates by an angle θ about the trailing edge and the rotation matrix is:

$$(x'_l, y'_l) = L \begin{bmatrix} \cos\theta & -\sin\theta \\ \sin\theta & \cos\theta \end{bmatrix} \begin{bmatrix} x_l \\ y_l \end{bmatrix} \tag{A-10}$$

$$R = \begin{bmatrix} \cos\theta & -\sin\theta \\ \sin\theta & \cos\theta \end{bmatrix} \tag{A-4}$$

In the proposed parametric model only the camber ratio m varies along the depth direction. The chord length L and pivot position C are constant. The variable m is modeled by a cubic B-spline curve with 7 control points. The control points are placed on the Y-Z plane. The points on the curve $P(t) = [P_y(t),$

But C is defined from the leading edge, and is different from the rotation center, as shown in Fig. A-2. Since the camber line is symmetric about $x = 0.5$, we can mirror the coordinate system
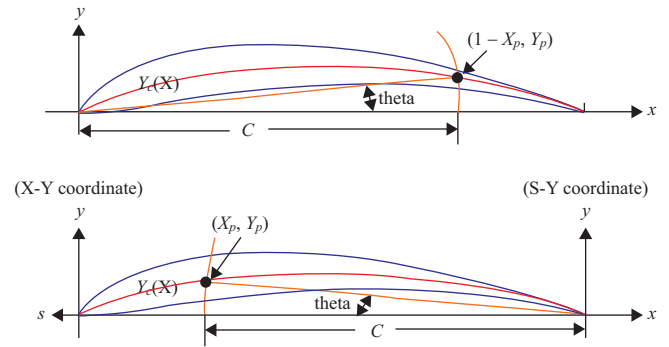
$P_z(t)$] represent the camber ratio $m = P_y(t)$ of the section at depth $P_z(t)$. Stacking the sections in parametric form the upper surface $f_u(s, t)$ and lower surface $f_l(s, t)$ can be defined as:

$$f_u(s,t) = \begin{bmatrix} L\cos\theta(1-s-y_t\sin\varphi) - L\sin\theta[4P_y(t)(s-s^2)+y_t\cos\varphi] \\ L\sin\theta(1-s-y_t\sin\varphi) + L\cos\theta[4P_y(t)(s-s^2)+y_t\cos\varphi] \\ P_z(t) \end{bmatrix} \quad \text{(A-11)}$$

$$f_l(s,t) = \begin{bmatrix} L\cos\theta(1-s+y_t\sin\varphi) - L\sin\theta[4P_y(t)(s-s^2)-y_t\cos\varphi] \\ L\sin\theta(1-s+y_t\sin\varphi) + L\cos\theta[4P_y(t)(s-s^2)-y_t\cos\varphi] \\ P_z(t) \end{bmatrix} \quad \text{(A-12)}$$

provided that:

$$\theta(t) = \tan^{-1} 4P_y(t)(1-C) \quad \text{(A-13)}$$

$$y_t(s) = \frac{T}{0.2}[0.2969(1-s)^{0.5} - 0.126(1-s) - 0.3516(1-s)^2 \\ + 0.2843(1-s)^3 - 0.1036(1-s)^4] \quad \text{(A-14)}$$

$$\varphi(s, t) = \tan^{-1} 4P_y(t)(2s-1) \quad \text{(A-15)}$$

REFERENCES

Abbott, I. H. and A. EvDoenhoff (1960.) Theory of Wing Sections: Including a Summary of Airfoil Data. New York: Dover Publications.

Carlton, J. S. (2012). Marine propellers and propulsion, London: Butterworth Heinemann, ch.13, Third Edition.

Carrica, P. M., A. M. Castro and F. Stern (2010). Self-propulsion computations using a speed controller and a discretized propeller with dynamic overset grids. Journal of Marine Science and Technology 15(4), 316-330.

Carrica, P. M., A. Mofidi, K. Eloot and G. Delefortrie (2016). Direct simulation and experimental study of zigzag maneuver of KCS in shallow water. Ocean Engineering 112, 117-33.

Castro, A. M., P. M. Carricaand F. Stern (2011). Full scale self-propulsion computations using discretized propeller for the KRISO container ship KCS.

Computers and Fluids 51(1), 35-47.

Çelik, F. and M. Güner (2007). Energy saving device of stator for marine propellers. Ocean Engineering 34(5), 850-855.

Chang, X., S. Sun,Y. Zhi and Y. Yuan (2018). Investigation of the effects of a fan-shaped Mewis duct before a propeller on propulsion performance. Journal of Marine Science and Technology, 1-14.

Chen, C. W., D. D. Kang, J. X. Leng, H. T. Lin, J. Wang, L. Jiao, Numerical Analysis on the Wake Field of Fast Container Ship Stern with Novel Propeller Duct (2014). IET Conference Publications, v 2014, n CP658, 2014, 2014 ISFMFE - 6th International Symposium on Fluid Machinery and Fluid Engineering.

Dawson, C. W. (1977). A practical computer method for solving ship-wave problems, Proceedings of the 2nd International Conference on Numerical Ship Hydrodynamics, 30-38.

Friedrich, M. and H. Uwe (2006). Special measures for improving propulsive efficiency, HSVA NewsWave 2006/1.

Gaggero, S., D. Villa and M. Viviani (2017). An extensive analysis of numerical ship self-propulsion prediction via a coupled BEM/RANS approach. APPLIED OCEAN RESEARCH 66, 55-78.

Grigoropoulos, G. J. and D. S. Chalkias (2010). Hull-form optimization in calm and rough water. Computer-Aided Design 42(11), 977-84.

Kim, H, J. Choi and H. Chun (2016). Hull-form optimization using parametric modification functions and particle swarm optimization. Journal of Marine Science and Technology 21(1), 129-44.

Kim, J., J. Choi, B. Choi, S. Chung and H. Seo (2015). Development of energy-saving devices for a full slow-speed ship through improving propulsion performance. International Journal of Naval Architecture and Ocean Engineering 7(2), 390-398.

Launder, B. E. and D. B. Spalding (1974). The numerical computation of turbulent flows. Computer Methods in Applied Mechanics and Engineering 3(2), 269-289.

Park S, G. Oh, S. Hyung Rhee, B. Koo and H. Lee (2015). Full scale wake prediction of an energy saving device by using computational fluid dynamics. Ocean Engineering 101, 254-263.

Robert, W. Fox, A. T. McDonald and P. J. Pritchard (2003). Introduction to FLUID MECHANICS (6th edn). John Wiley & Sons, Inc.

Tahara, Y., R. V. Wilson, P. M. Carrica and F. Stern (2006). RANS simulation of a container ship using a single-phase level-set method with overset grids and the prognosis for extension to a self-propulsion simulator. Journal of Marine Science and Technology 11(4), 209-228.

Thomas, L. and S. Heinrich (2009). Cavitation research on a very large semi spade rudder, Symposium on Marine Propulsors, Trondheim, Norway, June 2009.